Capitate-Based Kinematics of the Midcarpal Joint During Wrist Radioulnar Deviation: An *In Vivo* Three-Dimensional Motion Analysis

Hisao Moritomo, MD, Tsuyoshi Murase, MD, Akira Goto, MD, Kunihiro Oka, MD, Kazuomi Sugamoto, MD, Hideki Yoshikawa, MD, *Osaka, Japan*

Purpose: The purpose of this study was to obtain qualitative and quantitative information regarding *in vivo* 3-dimensional (3D) kinematics of the midcarpal joint during wrist radioulnar deviation (RUD).

Methods: We studied the *in vivo* kinematics of the midcarpal joint during wrist RUD in the right wrists of 10 volunteers by using a technology without radioactive exposure. The magnetic resonance images were acquired during RUD. The capitate was registered with the scaphoid, the lunate, and the triquetrum by using a volume registration technique. Animations of the relative motions of the midcarpal joint were created and accurate estimates of the relative orientations of the bones and axes of rotation (AORs) of each motion were obtained.

Results: The scaphoid, lunate, and triquetrum motions relative to the capitate during RUD were found to be similar, describing a rotational motion around the axis obliquely penetrating the head of the capitate in almost a radial extension/ulnoflexion plane of motion of the wrist. The AORs of the scaphoid, the lunate, and the triquetrum were located closely in space. In the axial plane the AORs of the scaphoid, lunate, and triquetrum formed a radially and palmarly opening angle of 43° ± 7°, 41° ± 11°, and 42° ± 14° with the wrist flexion/extension axis, respectively.

Conclusions: This study reports the *in vivo* 3D measurements of midcarpal motion relative to the capitate. Isolated midcarpal motion during RUD could be approximated to be a rotation in a plane of a radiodorsal/ulnopalmar rotation of the wrist, which may coincide with a motion plane of one of the most essential human wrist motions, known as the *dart-throwing motion*. (J Hand Surg 2004; 29A:668–675. Copyright © 2004 by the American Society for Surgery of the Hand.)

Key words: Capitate, kinematics, midcarpal joint, motion analysis, wrist.

From the Department of Orthopaedic Surgery, Osaka University Medical School, Osaka, Japan.

Received for publication October 22, 2003; accepted in revised form April 6, 2004.

Supported in part by Japan Society for the Promotion of Science Fujita Memorial Fund for Medical Research and grants-in-aid for Scientific Research, the Ministry of Education, Science, and Culture of Japan (H.M.).

No benefits in any form have been received or will be received from a commercial party related directly or indirectly to the subject of this article.

Reprint requests: Hisao Moritomo, MD, Department of Orthopaedic Surgery, Osaka University Medical School, 2-2, Yamadaoka, Suita-shi, Osaka, 565-0871 Japan.

0363-5023/04/29A04-0018$30.00/0
doi:10.1016/j.jhsa.2004.04.010

Note: To access the video accompanying this article, visit the July 2004 online issue of *Journal of Hand Surgery* at www.jhandsurg.org.

Understanding the interactions of the scaphoid, lunate, triquetrum, and the surrounding carpus is the key to how the wrist maintains its stability while allowing a large range of motion.[1] Although the traditional 2-dimensional radiographic studies of the wrist joint have tried to clarify kinematics of the radiocarpal joint,[2–5] kinematics of the midcarpal joint remain obscure. One reason is that it is very difficult to isolate the midcarpal motion radiographically during global wrist motion because the bones of both the proximal row and the distal row move relative to the radius so that one cannot observe the relative motion of the midcarpal joint. Although the previous studies using 3-dimensional (3D) motion analysis reported detailed data on the midcarpal motion,[6–8] most of the descriptions of the relative motion merely included a combination of numeric angles of simple motions based on the anatomic coordinate system, using terms such as *flexion, radial deviation,* or *pronation.* As a result the kinematics of midcarpal motion have remained obscure. It is difficult to assess 3D behavior of the midcarpal joint without visual information, such as 3D animation.

To overcome these problems in kinematic study, descriptions of the 3D carpal motions using computer-aided design models obtained from computed tomography have been developed.[9–11] These motion analysis systems enable the isolation and visualization of any motion of one bone relative to another bone. The 3D animation of the relative motion affords better appreciation of essential 3D kinematics through the visual check of the 3D motion. Moreover recent development of technology now has enabled *in vivo* motion analysis,[12–18] which would be expected to be more physiologic than *in vitro* motion analysis using cadavers. In a previous study we described the technical details of the *in vivo* 3D motion analysis and the kinematics of the triquetrum hamate joint.[18] The current study is a continuation of the previous study and was designed to investigate overall midcarpal kinematics during wrist radioulnar deviation (RUD) with increased number of observations.

Very little motion exists between the 4 bones of the distal row (trapezium, trapezoid, capitate, and hamate)[6,7,19] and that in contrast the 3 bones of the proximal row (scaphoid, lunate, and triquetrum) appear to be less tightly bound to one another.[2,7,20] Traditionally the midcarpal motion has been investigated by using the proximal body (scaphoid, lunate, and triquetrum) as a reference to determine the kinematics of a distal moving segment (the distal row). Although such a method affords detailed information on the relative motion between the distal and proximal rows, it still can be difficult to understand overall midcarpal motion. If the distal row (eg, capitate) is used as a reference to determine the kinematics of a proximal row (eg, scaphoid, lunate, and triquetrum) one can observe all the relative motions at the same time. Such capitate-based motion analysis may offer new information on the midcarpal kinematics. This study investigated the midcarpal motion in 2 ways: (1) the capitate motion relative to the scaphoid, lunate, and triquetrum, and (2) the scaphoid, lunate, and triquetrum motions relative to the capitate.

The purpose of this study was to obtain qualitative and quantitative kinematic information on the midcarpal joint during wrist RUD as well as its role in and contribution to global wrist motion.

Materials and Methods

The *in vivo* kinematics of the midcarpal joint during wrist RUD was studied in the right wrists of 10 volunteers (6 men, 4 women). The average age of the volunteers was 25 years (range, 20–32 y). The lunates were categorized as type 1 or type 2 based on the presence (type 2) or absence (type 1) of the medial hamate facet on the lunate in the midcarpal joint.[14] Whether the lunates were type 1 or type 2 was determined by measuring the coronal width of the hamate facet on the lunate in the coronal plane of the magnetic resonance image of the wrist in neutral position. There were 5 type 1 and 5 type 2 lunates (Table 1). Magnetic resonance images were acquired in 6 positions during RUD from 30° radial deviation to 45° ulnar deviation in 15° increments[18] in 5 wrists and acquired in 3 positions (a neutral position and 2 extreme positions) in the other 5 wrists. The contours of each bone were segmented from magnetic resonance volume images by using a software program (Virtual Place-M software program; Medical Imaging Laboratory, Tokyo, Japan) and surface models of the bones were constructed. The kinematic variables were calculated by registering the bone in one position and comparing it with another. The volume registration technique was used in this study. The iterative closest point algorithm[21] was used for registration in which a set of 3D volume points was registered by finding the best parameters, minimizing the sum of the distance from each 3D volume point. The scaphoid, the lunate, and the triquetrum were registered with the capitate to investigate the directions of the motion of the capitate relative to each of the bones in the proximal row. To compare the lo-

Table 1. Euler Angles of Motion of the Capitate Relative to the Scaphoid, Lunate, and Triquetrum From Ulnar Deviation to Radial Deviation

Case	Lunate Type	Age	Gender	Hamate Facet Width of the Lunate (mm)	Scaphoid			Lunate			Triquetrum		
					x	y	z	x	y	z	x	y	z
1	1	25	F	0	29.1°	−16.7°	3.1°	28.9°	−24.2°	8.0°	26.8°	−15.2°	8.5°
2	1	26	M	0	40.4°	−42.1°	3.6°	41.5°	−37.4°	5.0°	19.9°	−30.0°	15.7°
3	1	27	M	0	25.2°	−25.6°	−4.0°	38.6°	−28.2°	−3.3°	28.2°	−16.1°	−3.2°
4	1	24	M	0	23.0°	−24.4°	−0.5°	20.4°	−24.0°	−2.3°	9.6°	−21.8°	9.1°
5	1	24	M	0	33.7°	−37.5°	0.3°	36.6°	−33.8°	−0.5°	28.4°	−24.7°	−0.6°
Average of type 1 lunate					30.3°	−29.3°	0.5°	33.2°	−29.5°	1.4°	22.6°	−21.6°	5.9°
SD					7.0°	10.3°	3.1°	8.5°	5.9°	4.9°	8.0°	6.2°	7.7°
6	2	20	F	1.7	39.6°	−33.8°	5.8°	30.2°	−34.1°	7.0°	19.2°	−18.3°	16.8°
7	2	21	F	2.0	13.7°	−16.8°	7.2°	16.4°	−23.0°	5.7°	9.2°	−17.9°	10.8°
8	2	24	F	2.6	35.9°	−27.2°	1.7°	44.8°	−28.2°	1.1°	26.3°	−21.0°	−1.9°
9	2	25	M	4.2	28.5°	−32.2°	5.3°	30.6°	−27.9°	8.3°	21.2°	−22.4°	10.7°
10	2	32	M	4.3	26.0°	−23.3°	−7.7°	45.3°	−29.2°	−14.5°	35.0°	−17.5°	−13.2°
Average of type 2 lunate					28.7°	−26.7°	2.5°	33.5°	−28.5°	1.5°	22.2°	−19.4°	4.6°
SD					10.0°	6.9°	6.0°	12.0°	4.0°	9.4°	9.5°	2.2°	12.1°
Total average					29.5°	−28.0°	1.5°	33.3°	−29.0°	1.5°	22.4°	−20.5°	5.3°
SD					8.2°	8.4°	4.6°	9.8°	4.8°	7.0°	8.3°	4.5°	9.6°

x: +, extension; −, flexion; y: +, ulner deviation; −, radial deviation; z: +, supination; −, pronation.

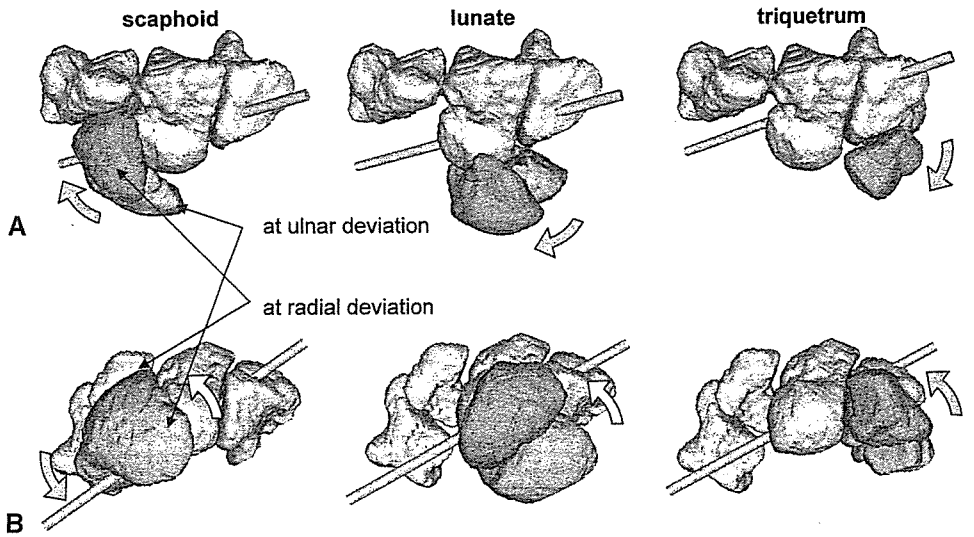

Figure 1. (A) Dorsal view and (B) proximal view of the capitate-based motions of the scaphoid, lunate, and triquetrum and their axes of rotation during RUD of the right wrist.

cation of the axes of rotation (AORs)[22] of the scaphoid, the lunate, and the triquetrum relative to the distal row, the capitate was registered with the scaphoid, the lunate, and the triquetrum. The coordinate system was constructed using bone landmarks in the neutral wrist position: the z-axis was defined as the long axis of the distal part of the radius, which was defined as the principal axis corresponding to the minimum moment of inertia. The x-axis was defined as a line passing the center of the capitate body at right angles to the z-axis and parallel to a line connecting the radial and ulnar styloid. The y-axis was defined as a line perpendicular to the other 2 axes.

Results

The Capitate Motion Relative to the Scaphoid, Lunate, and Triquetrum

From wrist ulnar deviation to radial deviation the capitate rotated radiodorsally relative to the scaphoid, the lunate, and the triquetrum. The converse was true during wrist ulnar deviation. The Euler angles of the capitate motion relative to the scaphoid, lunate, and triquetrum from the wrist ulnar deviation to wrist radial deviation are shown in Table 1. During wrist RUD the capitate angulated 28° ± 8° radially and 30° ± 8° dorsally relative to the scaphoid, 29° ± 5° radially and 33° ± 10° dorsally relative to the lunate, and 21° ± 5° radially and 22° ± 8° dorsally relative to the triquetrum. We could not find any significant difference in the Euler angles of the capitate motion relative to the scaphoid, lunate, and triquetrum between type 1 and type 2 lunates.

The Scaphoid, Lunate, and Triquetrum Motions Relative to the Capitate

On the capitate-based animation the scaphoid, lunate, and triquetrum motions relative to the capitate during RUD were found to be similar to each other, describing a rotational motion in a plane obliquely oriented relative to the coronal plane of the wrist that was almost a radial extension/ulnoflexion plane of the motion of the wrist (Figs. 1, 2A, 2B; video may be viewed at the *Journal's* Web site, www.jhandsurg.org). During wrist radial deviation the proximal portion of the scaphoid, the lunate, and the triquetrum moved radiodorsally and the distal portion of the scaphoid moved ulnopalmarly relative to the capitate. The converse was true during wrist ulnar deviation.

The AORs of the scaphoid, lunate, and triquetrum relative to the capitate were located closely together in space and ran obliquely from the radiopalmar aspect of the distal scaphoid to the ulnodorsal aspect of the hamate, penetrating the neck of the distal scaphoid and the waist of the capitate (Figs. 1, 3). In the axial plane the AORs of the scaphoid, lunate, and triquetrum formed a radially and palmarly opening angle of 43° ± 7°, 41° ± 11°, and 42° ± 14°, respectively, with the x-axis (flexion/extension axis) of the coordinate system (Fig. 3B).

The average range of motion of the scaphoid, the lunate, and the triquetrum around their own axes were 41° ± 10°, 44° ± 10°, and 33° ± 6°, respectively.There were relatively minor intercarpal motions between the scaphoid and the lunate and be-

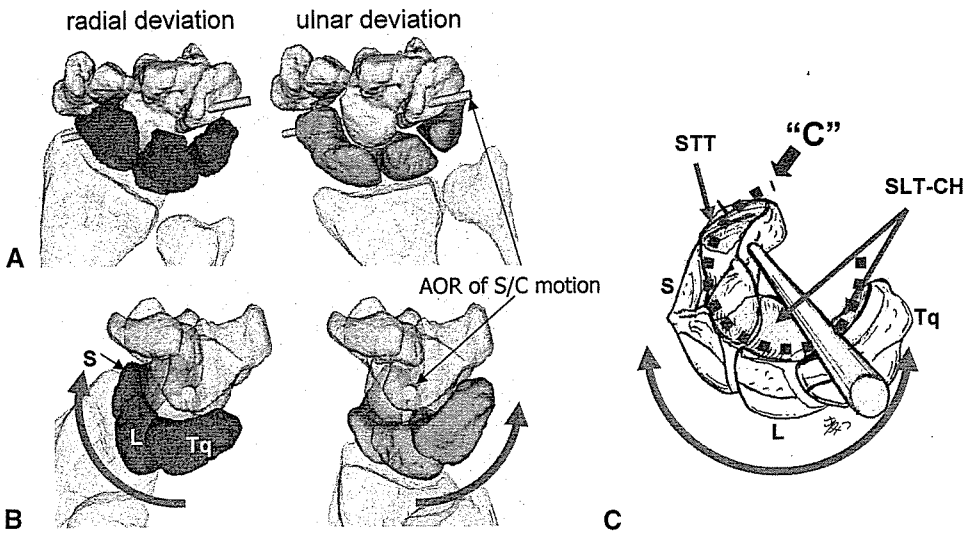

Figure 2. The capitate-based midcarpal motion during RUD. (A) Dorsal view. (B) Ulnodorsal view in which the AOR of the scaphoid-capitate (S/C) motion is perpendicular to the picture. (C) Schema of the ulnodorsal view of the proximal row. The outlines of the surfaces of the STT and SLT-CH joints form a C shape.

tween the lunate and the triquetrum, averaging 8° ± 6° and 16° ± 5°, respectively.

We could not find any significant difference in these AORs and range of motions of the scaphoid, lunate, and triquetrum relative to the capitate between type 1 and type 2 lunates.

Discussion

Current kinematic technique has some limitations. The biggest disadvantage of this technique is that it makes a static rather than dynamic motion analysis. Static measurement does not include any inertial or functional effects that might occur during normal wrist motion. This technique, however, can provide new information regarding *in vivo* midcarpal kinematics.

The midcarpal joint is a major component of the wrist joint and substantially contributes to overall global wrist motion. The scaphotrapeziotrapezoid (STT) joint[10,23] and the triquetrum-hamate (TqH) joint[18] have been studied by one of the current authors (H.M.), both anatomically and kinematically. The studies of the STT joint revealed that the skeletal and ligamentous constraints of the STT joint are very strong and the STT joint essentially has a single degree of freedom. The studies of the STT joint also revealed that the AOR of the STT joint runs obliquely from radiopalmar to ulnodorsal,[10] which is consistent with the current *in vivo* study. The study of the TqH joint revealed that the triquetrum rotated obliquely relative to the hamate during wrist RUD in a radial extension/ulnoflexion plane of motion. This suggests that the TqH motion is similar to the STT motion. The present study suggests that the lunate motion relative to the capitate is also very similar to that of the STT and TqH motions. Collectively this

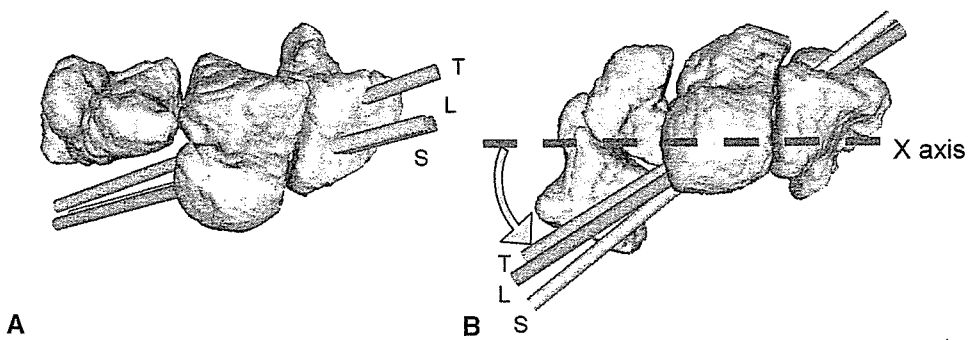

Figure 3. (A) Dorsal view and (B) proximal view of the distal row of the right wrist and the axes of rotation of the scaphoid (S), lunate (L), and triquetrum (T). x-axis, wrist flexion/extension axis.

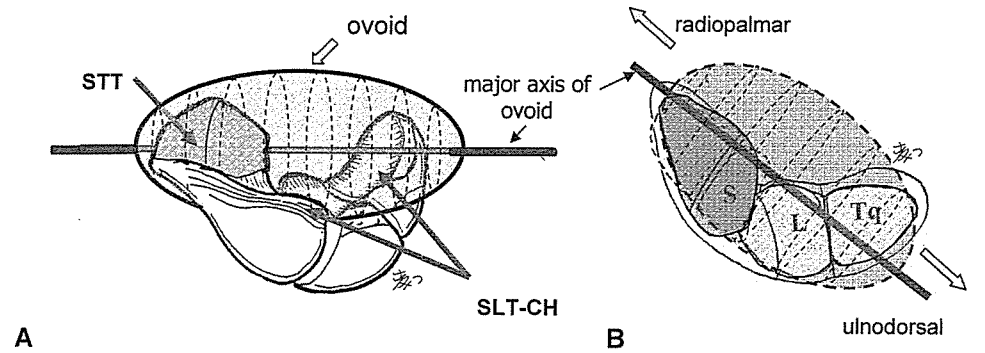

Figure 4. (A) Radiodorsal and (B) distal views of the proximal row and an ovoid. Most of the joint surfaces of the midcarpal joint contact with the imaginary ovoid, whose major axis run obliquely from radiopalmar to ulnodorsal. S, scaphoid; L, lunate.

information implies that the midcarpal motion during RUD is more synchronous than previously reported.

From an anatomic point of view the midcarpal joint may have the most complicated joint shape in the human body. In a broad sense there are 2 articulations: the STT joint and the scapholunotriquetrum-capitate-hamate (SLT-CH) joint. The former is convex proximally whereas the latter is concave. Two-dimensionally these joints form an S shape in a posteroanterior x-ray, which has made the kinematics of the midcarpal joint difficult to understand. Through 3D analysis of the anatomy and kinematics of the midcarpal joint it appears that most of the joint surface of the midcarpal joint forms an ovoid whose major axis runs obliquely from radiopalmar to ulnodorsal (Fig. 4). The STT joint contacts the radiodistal part of the ovoid and the SLT-CH joint contacts the proximal and ulnar parts of the ovoid. Thus the shape of the midcarpal joint allows this joint to rotate smoothly and congruently in an oblique plane of wrist radiodorsal/ulnopalmar rotation around the major axis of the ovoid, which runs obliquely from radiopalmar to ulnodorsal.

The major axis of this ovoid appears to be located closely in space to the AORs of the scaphoid-capitate joint, as determined in this study (Fig. 2). In an oblique view from the dorsoulnar side of the wrist where the AOR of the scaphoid-capitate joint is perpendicular to the picture, the outlines of the surfaces of the STT and SLT-CH joints are seen to form a three-quarter circle or a C shape (Figs. 2B, 2C). The center of the C appears to coincide with the major axis of the ovoid.

Applying this ovoid/C-shaped concept to the kinematics of the midcarpal joint it appears that essentially the kinematics of the midcarpal joint during RUD are a radiodorsal/ulnopalmar rotation around the AOR of the scaphoid-capitate joint, which passes through the center of the C shape of the 3D joint surface contacts of the midcarpal joint (Fig. 2B; video may be viewed at the *Journal's* Web site, www.jhandsurg.org). Therefore we may reasonably conclude that essential kinematics of the midcarpal joint during RUD could be approximated to be a radiodorsal/ulnopalmar rotation around the AOR of the scaphoid-capitate joint along with the C shape of the joint surface of the midcarpal joint.

This radiodorsal/ulnopalmar rotation coincides

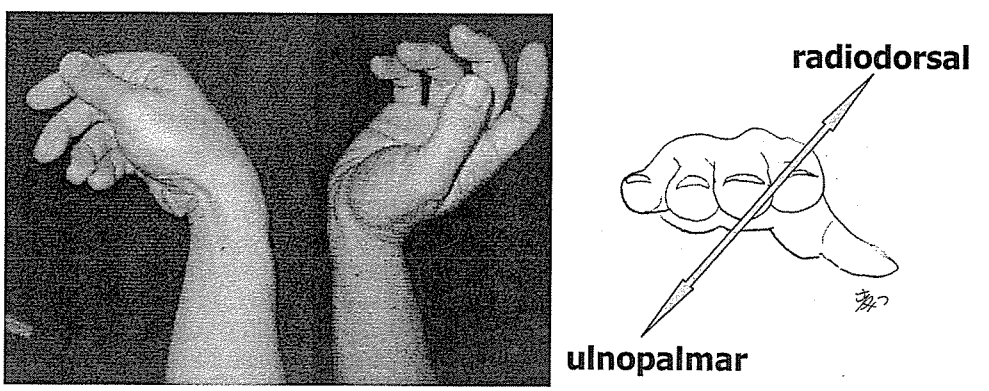

Figure 5. Dart-throwing motion (wrist radiodorsal/ulnopalmar rotation).

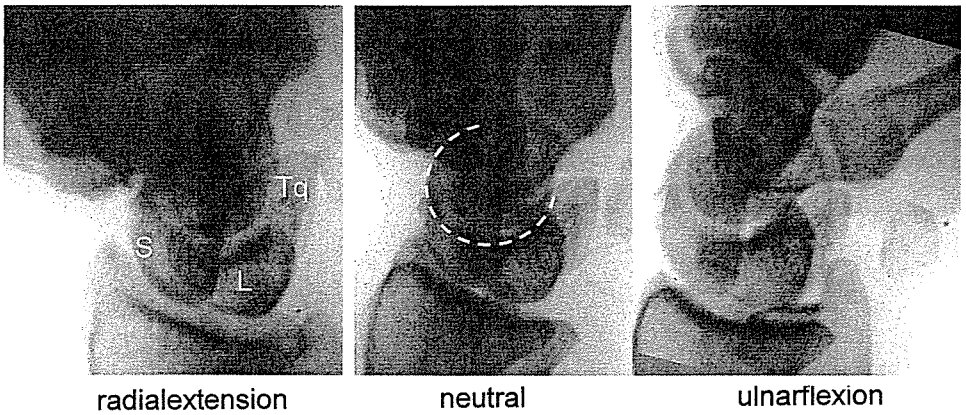

Figure 6. The C shape of the outlines of the midcarpal joint surface can be seen radiographically when the x-ray beam is aligned along the radiodorsal/ulnopalmar axis of the dart-throwing motion in the semisupinated view. S, scaphoid; L, lunate.

with the so-called dart-throwing motion[24,25] (wrist radiodorsal/ulnopalmar rotation, Fig. 5), which is one of the most frequently used wrist motions in activities of daily living such as hammering nails, beating a drum, swinging a golf club, or casting a fishing rod. The C shape of the outlines of the midcarpal joint surface can be seen radiographically when the x-ray beam is aligned along the radiodorsal/ulnopalmar axis of the dart-throwing motion in the semisupinated view (Fig. 6). Radiodorsal/ulnopalmar rotation may be the most stable and controllable human wrist motion, which is the main motion plane of the midcarpal joint.

Nakamura et al[26] reported that the kinematics of the type 1 lunate are different from those of a type 2 lunate in 2-dimensional study although we could not find any notable difference in their midcarpal behavior between type 1 and type 2 lunates. We speculate that may be owing to the innate limitation of the 2-dimensional measurements, which are influenced more by the shape of the lunate than our 3D measurement using Euler angle. We probably need to increase the number of subjects, however, to conclude this matter.

This study suggests that the midcarpal joint may be much more important than previously suggested in terms of its contribution to both the stability and mobility of the global wrist joint. Furthermore this raises concern regarding the impact of partial or complete fusion of the midcarpal joint on overall wrist motion and stability. We hope the information and ovoid/C-shape perspective of the anatomy and kinematics of the midcarpal joint will assist the clinician in better understanding the wrist joint and some of its disorders.

The authors acknowledge the assistance during parts of the experimental procedure from Yoshinobu Sato, PhD, from the Department of Medical Robotics and Image Sciences, Osaka University Graduate School of Medicine; Takehiro Arimura, RT, from the Department of Radiology, Osaka University Graduate School of Medicine; and from Ryoji Nakao (MMT Co.).

References

1. Weber ER. Concepts governing the rotational shift of the intercalated segment of the carpus. Orthop Clin North Am 1984;15:193–207.
2. Kauer JM. The interdependence of carpal articulation chains. Acta Anat (Basel) 1974;88:481–501.
3. Sarrafian SK, Melamed JL, Goshgarian GM. Study of wrist motion in flexion and extension. Clin Orthop 1977;126:153–159.
4. Schuhl JF, Leroy B, Comtet JJ. Biodynamics of the wrist: radiologic approach to scapholunate instability. J Hand Surg 1985;10A:1006–1008.
5. Nakamura R, Hori M, Imamura T, Horii E, Miura T. Method for measurement and evaluation of carpal bone angles. J Hand Surg 1989;14A:412–416.
6. de Lange A, Kauer JM, Huiskes R. Kinematic behavior of the human wrist joint: a roentgen-stereophotogrammetric analysis. J Orthop Res 1985;3:56–64.
7. Ruby LK, Cooney WP III, An KN, Linscheid RL, Chao EY. Relative motion of selected carpal bones: a kinematic analysis of the normal wrist. J Hand Surg 1988;13A:1–10.
8. Kobayashi M, Berger RA, Nagy L, Linscheid RL, Uchiyama S, Ritt M, et al. Normal kinematics of carpal bones: a three-dimensional analysis of carpal bone motion relative to the radius. J Biomech 1997;30:787–793.
9. Patterson RM, Nicodemus CL, Viegas SF, Elder KW, Rosenblatt J. High-speed, three-dimensional kinematic analysis of the normal wrist. J Hand Surg 1998;23A:446–453.
10. Moritomo H, Viegas SF, Elder K, Nakamura K, Dasilva MF, Patterson RM. The scaphotrapezio-trapezoidal joint. Part 2: a kinematic study. J Hand Surg 2000;25A:911–920.
11. El-Shennawy M, Nakamura K, Patterson RM, Viegas SF. Three-dimensional kinematic analysis of the second through fifth carpometacarpal joints. J Hand Surg 2001;26A:1030–1035.

12. Wolfe SW, Crisco JJ, Katz LD. A non-invasive method for studying in vivo carpal kinematics. J Hand Surg 1997;22B: 147–152.
13. Crisco JJ, McGovern RD, Wolfe SW. Noninvasive technique for measuring in vivo three-dimensional carpal bone kinematics. J Orthop Res 1999;17:96–100.
14. Feipel V, Rooze M. Three-dimensional motion patterns of the carpal bones: an in vivo study using three-dimensional computed tomography and clinical applications. Surg Radiol Anat 1999;21:125–131.
15. Snel JG, Venema HW, Moojen TM, Ritt JP, Grimbergen CA, den Heeten GJ. Quantitative in vivo analysis of the kinematics of carpal bones from three-dimensional CT images using a deformable surface model and a three-dimensional matching technique. Med Phys 2000;27:2037–2047.
16. Wolfe SW, Neu C, Crisco JJ. In vivo scaphoid, lunate, and capitate kinematics in flexion and in extension. J Hand Surg 2000;25A:860–869.
17. Neu CP, Crisco JJ, Wolfe SW. In vivo kinematic behavior of the radio-capitate joint during wrist flexion-extension and radio-ulnar deviation. J Biomech 2001;34:1429–1438.
18. Moritomo H, Goto A, Sato Y, Sugamoto K, Murase T, Yoshikawa H. The triquetrum-hamate joint: an anatomic and in vivo 3-dimensional kinematic study. J Hand Surg 2003; 28A:797–805.
19. Savelberg HH, Otten JD, Kooloos JG, Huiskes R, Kauer JM. Carpal bone kinematics and ligament lengthening studied for the full range of joint movement. J Biomech 1993;26:1389–1402.
20. Seradge H, Sterbank PT, Seradge E, Owens W. Segmental motion of the proximal carpal row: their global effect on the wrist motion. J Hand Surg 1990;15A:236–239.
21. Besl PJ, Mackay N. A method for registration of 3-D shapes. IEEE Trans Patt Anal Mach Intell 1992;14:239–256.
22. Panjabi MM, Krag MH, Goel VK. A technique for measurement and description of three-dimensional six degree-of-freedom motion of a body joint with an application to the human spine. J Biomech 1981;14:447–460.
23. Moritomo H, Viegas SF, Nakamura K, Dasilva MF, Patterson RM. The scaphotrapezio-trapezoidal joint. Part 1: an anatomic and radiographic study. J Hand Surg 2000;25A: 899–910.
24. Saffar P, Semaan I. The study of the biomechanics of wrist movements in an oblique plain—a preliminary report. In: Schuind F, An KN, Cooney WP, Garcia-Elias M, eds. Advances in the Biomechanics of the Hand and Wrist. New York: Plenum Press, 1994:305–311.
25. Ishikawa J, Cooney WP 3rd, Niebur G, An KN, Minami A, Kaneda K. The effects of wrist distraction on carpal kinematics. J Hand Surg 1999;24A:113–120.
26. Nakamura K, Beppu M, Patterson RM, Hanson CA, Hume PJ, Viegas SF. Motion analysis in two dimensions of radioulnar deviation of type 1 versus type 2 lunates. J Hand Surg 2000;25A:877–888.

In vivo elbow biomechanical analysis during flexion: Three-dimensional motion analysis using magnetic resonance imaging

Akira Goto, MD,[a] Hisao Moritomo, MD,[b] Tsuyoshi Murase, MD,[b] Kunihiro Oka, MD,[b] Kazuomi Sugamoto, MD,[a] Takehiro Arimura,[c] Yoshikazu Nakajima, PhD,[d] Takaharu Yamazaki,[d] Yoshinobu Sato, PhD,[d] Shinichi Tamura, PhD,[d] Hideki Yoshikawa, MD,[b] and Takahiro Ochi, MD,[a] *Suita, Japan*

The purpose of this article is to evaluate in vivo 3-dimensional kinematics of the elbow joint during elbow flexion. We studied the ulnohumeral and radiohumeral joint noninvasively in 3 elbows in healthy volunteers using a markerless bone registration algorithm. Magnetic resonance images were acquired in 6 positions of elbow flexion. The inferred contact areas on the ulna against the trochlea tended to occur only on the medial facet of the trochlear notch in all of the elbow positions we tested. The inferred contact areas on the radial head against the capitellum occurred on the central depression of the radial head in all of the tested elbow positions except for 135° flexion, where the anterior rim of the radial head articulates with the capitellum. (J Shoulder Elbow Surg 2004;13:441–7.)

Motion analysis has been widely used to study normal and pathologic kinematics and the effects of reconstructive procedures on pathologic conditions. Kinematic data have been mainly obtained in vitro by a variety of techniques, including bipolar radiography,[11,19,20] electromagnetic sensors,[8] and high-speed video data acquisition systems.[15,18] These methods rely on the assumption that the movement of the markers truly mimics the motion of the bone. These techniques use invasive procedures to mount markers on the bones, such as transcutaneous bone pins or implantable bone markers. As a result, the utility of bone markers is further compromised by mechanical impingement and tethering of soft tissues. Moreover, in vitro experiments cannot completely reproduce the physical muscular force across the elbow. This limitation may alter normal kinematics.

Recently, researchers have been able to measure 3-dimensional (3D) in vivo kinematics using noninvasive techniques. These techniques use surface-based registration of the bones to determine corresponding relationships between images represented at different coordinates via computed tomography (CT) or magnetic resonance imaging (MRI).[1,3] By use of this methodology, in vivo 3D kinematics of the elbow joint can be analyzed noninvasively.

Accurate measurement of the contact areas of the elbow has been extremely difficult, and several techniques have been applied to this highly congruous joint.[21] Silicone casting[4,6] and reversible cartilage staining[7] in studies with cadaveric models have been most commonly used. Again, in vitro experiments cannot reproduce completely the physical muscular force across the elbow, which undoubtedly influences the resulting contact areas. Using a proximity mapping technique,[14] however, we can calculate the in vivo inferred contact area of the elbow joint noninvasively from bone surface models created from CT or magnetic resonance (MR) images. This technique extends our functional understanding of the elbow.

The purpose of this article is to evaluate in vivo 3D kinematics of the elbow joint during flexion motion. We especially focused on the contact areas of the ulnohumeral and radiohumeral joint. In addition, we investigated the pathway of the helical screw axis of motion of the ulna relative to the humerus and the change in the carrying angles with elbow flexion for the ulnohumeral joint.

MATERIALS AND METHODS

We studied the right elbow joints of 3 healthy volunteers (1 woman and 2 men; age range, 24-26 years; mean age, 25.0 years) during elbow flexion motion. The steps in 3D registration are image acquisition, segmentation, and registration. A mathematical description of the motion of individual bones and of their relative motion is derived by

From the Division of Robotic Therapy,[a] Department of Orthopaedic Surgery,[b] and Division of Interdisciplinary Image Analysis, Osaka University Graduate School of Medicine,[c] and Department of Radiology, Osaka University Hospital.[d]

Reprint requests: Akira Goto, MD, Department of Orthopaedic Surgery, Osaka University Graduate School of Medicine, 2-2 Yamadaoka, Suita 565-0871, Japan (E-mail: *goto-akira@umin.ac.jp*).

1058-2746/2004/$30.00
doi:10.1016/j.jse.2004.01.022

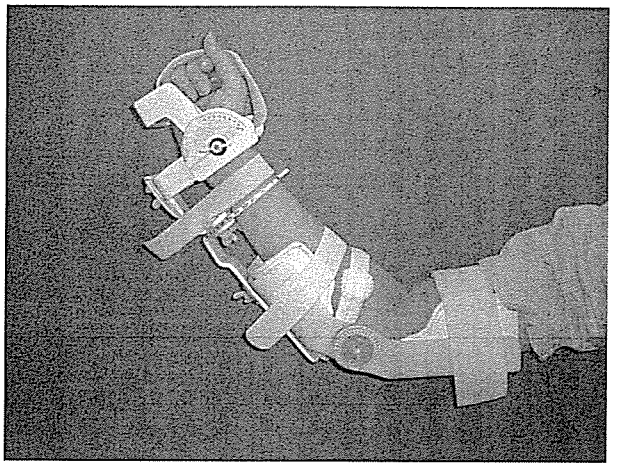

Figure 1 To immobilize the elbow and the wrist at a specific angle during flexion-extension, a special posture device was designed.

computing the rigid transformation required to match the surface models.

Image acquisition

MRI data of the right elbows of volunteers were obtained with a 1.5-T commercial MR system (Magnetom Vision Plus 1.5-T MRI; [Siemens AG, Erlangen, Germany]) in conjunction with a receive-only body-array surface coil. We used a 3D sequence (3dflash) with a TR/TE/flip angle of 2.3 milliseconds/33 milliseconds/45°, a 256 × 200 in-plane acquisition matrix, and a 350-mm field of view and 2.0-mm thickness on a contiguous slice with a pixel size of 0.6 × 0.8 mm. Acquisition of a 3D volume image requires approximately 5 minutes. To immobilize the elbow and the wrist at a specific angle during flexion-extension, a special posture device was designed. During this study of elbow flexion, the forearm was fixed in the neutral position (Figure 1). Each volunteer was positioned in a semiprone position, and images were obtained in 6 positions of elbow flexion (0°, 30°, 60°, 90°, 120°, and 135°).

Segmentation

Segmentation was defined as extracting bone contours and associating each contour with the individual bones. The contours of each bone were segmented from MR volume images by use of the Virtual Place-M software program developed in our laboratory (Medical Imaging Laboratory, Tokyo, Japan). Surface models of the humerus, ulna, and radius were obtained by applying a 3D surface generation of the bones' cortex. By means of the graphics workstation, the 3D geometry of each bone was obtained by connecting the different sections. The software generated 3D surface bone models via the marching cubes technique.[13] Visualization of the geometrical models of each elbow was obtained by use of the software program developed in our laboratory (Division of Functional Diagnostic Imaging, Biomedical Research Center, Osaka University Medical School, Suita, Japan).

Registration

Registration was performed under the assumption that each bone moved independently as a rigid body 3-dimensionally. The kinematic variables were calculated by registering the bone, described by its surface points obtained from segmentation, from one position to another position. We used the iterative closest point algorithm,[1] which is one of the most well-developed methods for surface-based registration. In this method, a 3D surface model and a set of 3D points are registered by starting from initial transformation parameters and finally finding the best parameters while minimizing the sum of the distance from each 3D point to the surface. The humerus was registered with the ulna and the radius. The relative motions between the humerus and the ulna and between the humerus and the radius were determined with this technique.

Motion analysis

This system enables one to view and analyze any bone motion relative to any other bone. Using motion analysis, we calculated several measurements that were hypothesized to characterize elbow motion. The measurements obtained were inferred contact areas with their area centroids, the screw axis of rotation between bones, and the carrying angles. This system serves as a visual check by which to validate the resulting calculated motion of the bones, as well as providing a simple, clear manner by which to display the analyst's conclusions.

Contact area

We measured the inferred contact area of the ulnohumeral and radiohumeral joints using a proximity mapping method[14] during different elbow positions. Proximity mapping to demonstrate distances between 3D surface bone models was accomplished by use of 3D MRI. To determine the interbone distances, a custom program was created. This program used the output file from the solid model formation (3D reconstructions), which gives all vertices positions of the individual surface triangles that form the surface of the reconstructed bone in space. The vertices of the triangles were used as discrete bony landmarks and as a starting point for the minimum distance estimation between bones. From a specific vertex, the algorithm searches all other vertices within a slice and calculates each distance, retaining the minimum distance. If the distance between slices is less than the minimum distance already calculated, the algorithm calculates distances to points in the adjacent slice in search of the minimum; otherwise, that intraslice minimum distance is kept and the next vertex distance is calculated. An output file is created that contains the minimum distance for each vertex and the adjacent bone to which it corresponds. This program was written for the calculation of both the area and centroid of one bone surface with respect to another within a user-specified threshold distance. Proximity mapping is the visual representation of the distance from one bone to the nearest neighboring bone. This method can be used to determine the interbone distances and the centroid of the mapping area. Surface proximity mapping that infers contact area between joint surfaces and their area centroids was calcu-

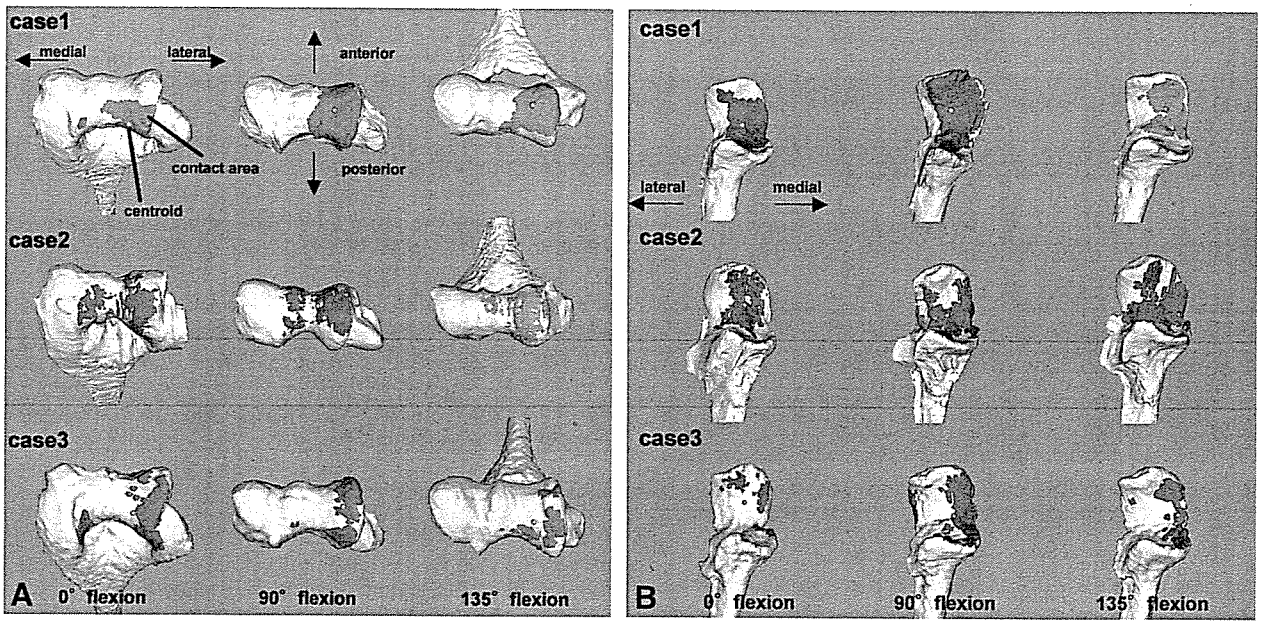

Figure 2 The inferred contact areas of articular surfaces and their centroids of the ulnohumeral joint in 0°, 90°, and 135° flexion. **A**, Contact areas on the humerus. **B**, Contact areas on the ulna.

lated from 3D MR images to visualize the path of motion of the ulna and the radius on the humerus during flexion. The proximity maps were calculated within 2.0- to 3.0-mm distant thresholds according to the size of the individual joint.

Axis of rotation

We expressed the transformations in helical axis parameters, which are defined as a rotation about and a translation along a unique axis.[17] Screw axes of rotation were calculated for each increment of motion. We depicted the configuration and dimensions of these axes. To measure changes of the respective axes, we calculated angular variances from respective subject helical axes in the axial and coronal plane, the minimum distances between the respective axes, and the orientation of the average axis. Screw axes were calculated only for the ulnohumeral joint, because the radiohumeral joint possesses two degrees of freedom of motion (flexion/extension and pronation/supination) and we could not completely exclude pronation/supination motion during an experiment for flexion/extension motion.

Carrying angle

To investigate changes in the carrying angle 3-dimensionally, we defined the carrying angle as the abduction-adduction angle of the long axis of the ulna with respect to the sagittal plane, and we calculated the angle analytically based on the new reference system. The geometrical center of mass and the principal axes of inertia were calculated for each 3D volume of the distal third of the humerus and the proximal third of the ulna. The principal axes of inertia are defined as the long axis, which corresponds to the minimum moment of inertia; the short axis, which corresponds to the maximum moment of inertia; and the medium axis, which is perpendicular to both the long and short axes. The short axes of inertia of the volumes correspond to the anatomic long axes of the humerus and the ulna. The new reference system was defined by use of the principal axes of inertia of the humerus. The sagittal plane was defined as a plane containing the long and short axes of inertia of the humerus. Thus, the precise angle was calculated for each angle of flexion for each elbow.

Validation of registration

The accuracy and consistency of the in vivo methodology described here were determined preliminarily in an in vitro study. MRI scans of a fresh cadaveric arm were acquired three times, changing only the direction of the MR image slices. Reconstructed 3D models of the humerus and radius were created separately from each set of MRI data. The relative position of the radius to the humerus was calculated and was compared among the three MRI slices. It was revealed that our method had a mean rotation error of 0.82° ± 0.38°, a mean translation error of 0.04 ± 0.01 mm, and a mean consistency of 0.32 ± 0.11 mm (root mean square). Therefore, both the segmentation error and the range of MRI acquisition resolutions that might have potentially influenced the results were revealed to be very small.

RESULTS

Contact area

The inferred contact areas of articular surfaces and their centroids of the ulnohumeral joint in 0°, 90°, and 135° flexion are shown in Figure 2. On the humerus, most of the contact areas on the trochlear surface are

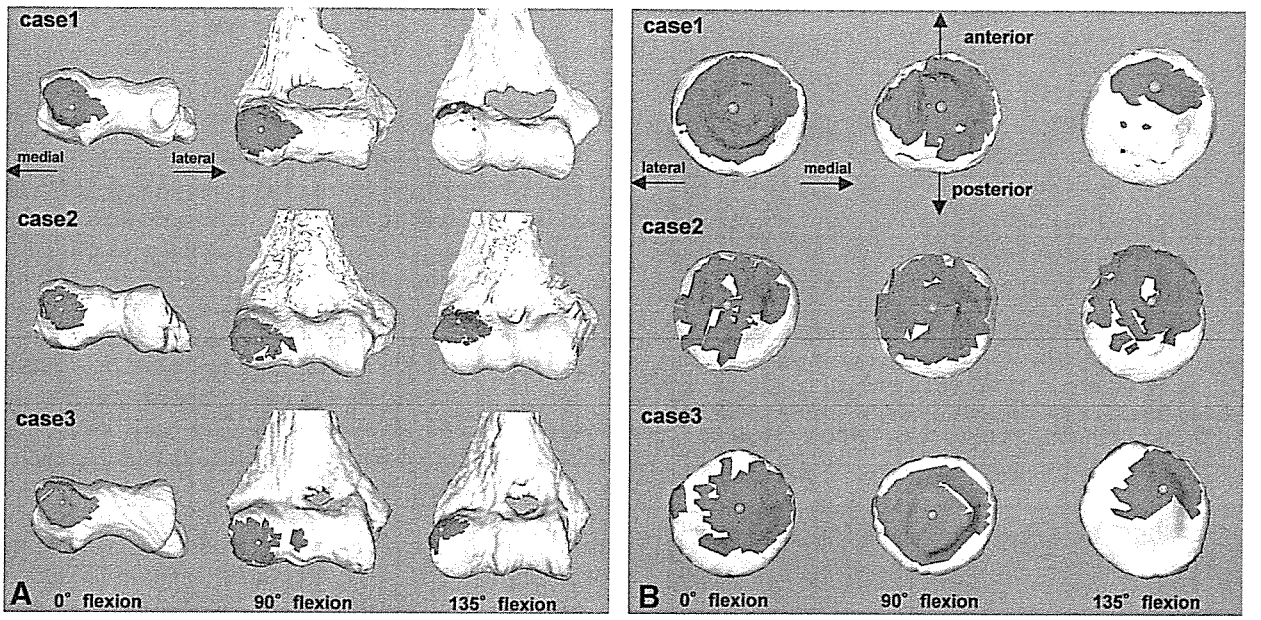

Figure 3 The inferred contact areas of articular surfaces and their centroids of the radiohumeral joint in 0°, 90°, and 135° flexion. **A**, Contact areas on the humerus. **B**, Contact areas on the radius.

situated on the medial facet of the trochlea for any possible elbow position. On the ulna, the contact areas also tended to occur medially in all different elbow positions. The pathway of the area centroids of the contact areas in the ulnohumeral joint during flexion is situated on the medial face of the trochlea just lateral to the sulcus of the trochlear groove.

The inferred contact areas of articular surfaces and their centroids of the radiohumeral joint in 0°, 90°, and 135° flexion are shown in Figure 3. Contacts on the capitellar surface were observed to move linearly from the lower aspect of the capitellum in 0° flexion to the upper aspect in 135° flexion. The inferred contact areas on the radial head against the capitellum occurred on the central depression of the radial head during all different elbow positions except 135° flexion, where the anterior rim of the radial head articulates with the capitellum (Figure 4). The pathway of the area centroids of the contact areas in the radiohumeral joint is situated along a slightly oblique line from the lower medial aspect to the upper lateral aspect on the capitellum with flexion.

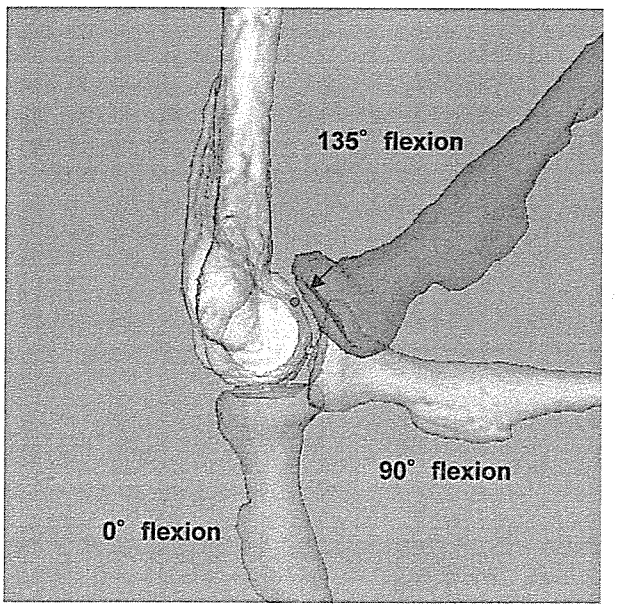

Figure 4 Lateral view of the radiohumeral joint in 0°, 90°, and 135° flexion with their centroids of the contact areas. Note that the anterior rim of the radial head articulates with the capitellum in 135° flexion (*arrow*).

Axis of rotation of motion of ulna relative to humerus

The pathway of the screw axis of rotation exhibits a roller configuration tracing the surface of a double conic shape, with the frustum waist being located in the medial portion of the trochlea (Figure 5). The locus of the axis of rotation traced on the surface of the condyles tended to be larger on the lateral side than on the medial side. The locus of the averaged axis of rotation on the lateral condyle showed a counterclockwise circular pattern (Figure 6). The screw axis of rotation varied from 5.67° to 17.23° (mean, 11.02°) in the axial plane and from 7.80° to 19.4° (mean, 11.95°) in the coronal plane. The minimum distances between the respective axes were 0.439 to 0.863 mm (mean, 0.685 mm). All screw axes of

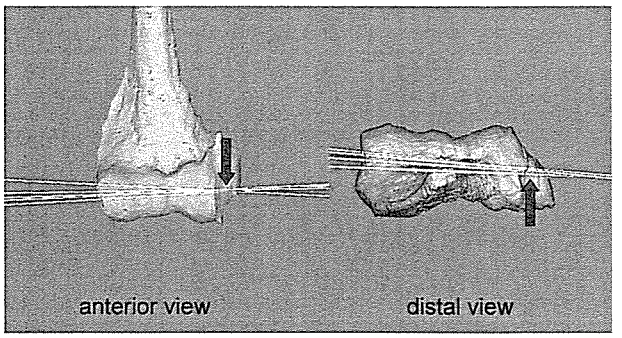

Figure 5 Superimposed images of the instantaneous axes of rotation of the ulnohumeral joint showing roller configuration tracing the surface of a double conic shape, with the frustum waist being located in the medial portion of the trochlea (*arrows*).

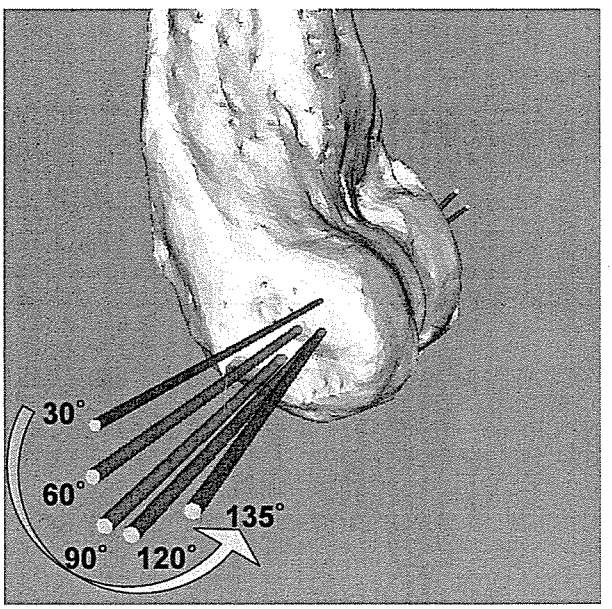

Figure 6 The locus of the averaged axis of rotation on the lateral condyle shows a counterclockwise circular pattern, where it initially moves anteriorly in the range from 0° to 60° flexion and then returns posteriorly.

rotation nearly intersected on the medial facet of the trochlea. The calculated average axis among all positions penetrated the inferior anterior aspect of the medial epicondyle, the center of the trochlea, and the center of the capitellum. In the coronal plane, the average axis formed a proximally and laterally opening angle of 85.46° (SD, 1.55) with the longitudinal axis of the humerus.

Carrying angle

The carrying angle in 0° flexion varied from 16.04° to 22.78° (mean, 18.64°). The pattern of change in the carrying angles with elbow flexion for the ulnohumeral joint was consistent in all elbows. The averaged carrying angle decreased linearly with flexion (Figure 7).

DISCUSSION

This study represents an attempt to analyze 3D motion of the elbow in vivo and noninvasively. We used MRI to avoid radiation exposure from radiographic imaging or CT scanning. Some previous studies were 2-dimensional kinematic analyses, and the importance of documenting 3D kinematics has been noted.[2] In addition, most of the present knowledge about 3D behavior of the skeletal joints has been acquired in studies of cadaveric models using invasive procedures. In vitro studies are also inherently limited because if joint loading with muscular forces is to be accounted for, they must be estimated and simulated. It has been proposed that small changes in joint loading may have profound effects on joint kinematics.[23]

This in vivo analysis offers 3D measurements gathered by use of many different methodologies. With the use of surface registration techniques,[1,3] the 3D quantitative information regarding relative displacement and rotation was acquired in vivo and noninvasively without bone markers. This technique can be used for accurate computer visualization of experimental kinematics by use of the surface models of the bones derived from the MRI data.

The ulnohumeral joint is generally described as a hinge joint.[12] A previous study showed that flexion occurs about a single axis, which passes through the centers of the arcs outlined by the bottom of the trochlear sulcus and the periphery of the capitellum. More recent studies have shown that the elbow joint does not function as a simple hinge joint and that the joint axis translates as well as rotates.[22] The respective axis intersects the trochlear center medially, and the axes translate more at the lateral side than at the medial side.[5] In our studies the results agree well with these findings. These results may suggest the importance of the function of the medial collateral ligament, and they are consistent with the findings about the relatively ambiguous anatomy of the lateral collateral ligament.

The previous studies showed that the change in carrying angle during elbow flexion is linear, being greatest at 0° flexion and diminishing during flexion.[16,24] Our results also agree well with these findings.

A review of the literature has shown that only a few in vitro studies have been performed to obtain data on elbow joint contact. Previous in vitro studies showed that the contact areas on the ulna occurred anteriorly and posteriorly, forming two narrow bands.[4,7] Goel et al[6] reported that in 0° flexion, the contact was observed to be on the lower medial

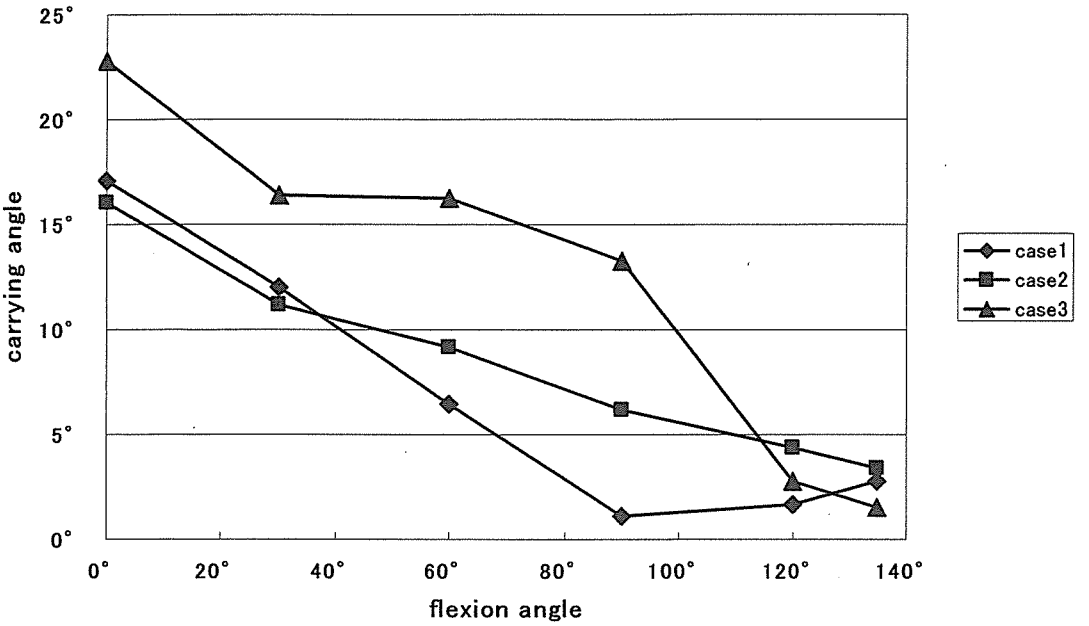

Figure 7 The change in the averaged carrying angle with elbow flexion for the ulnohumeral joint, which decreases linearly.

aspect of the ulna, whereas in other postures, the pressure areas described a strip extending from posterolateral to anteromedial. In our in vivo studies, the pattern of the contact area is different from that observed in the previous in vitro reports. On the ulna, most of the inferred contact areas with the trochlea occurred only on the medial facet of the trochlear notch in all different elbow positions. The path of the centroids of contact areas across the trochlea was revealed to be not on the sulcus but on the medial facet of the trochlea.

Although current techniques provide a detailed analysis of the in vivo kinematics of elbow motion, they have some limitations, with the greatest disadvantage being the use of static motion analysis rather than dynamic analysis, such as instrumented spatial linkages.[9,10] Dynamic kinematic factors such as muscle were not considered in this methodology. The proximity mapping technique has an inherent limitation because of its lack of consideration of thickness of the cartilage. Furthermore, we cannot yet make a definitive statement about elbow kinematics because our database is still small. Additional research is required to build the database.

REFERENCES

1. Besl PJ, Mackay N. A method for registration of 3-D shapes. IEEE Trans Patt Anal 1992;14:239-56.
2. Bottlang M, Madey SM, Steyers CM, Marsh JL, Brown TD. Assessment of elbow joint kinematics in passive motion by electromagnetic motion tracking. J Orthop Res 2000;18:195-202.
3. Crisco JJ, McGovern RD, Wolfe SW. Three-dimensional joint kinematics using bone surface registration: a computer assisted approach with an application to the wrist joint in vivo. MICCAI 1998:696-9.
4. Eckstein F, Lohe F, Muller-Gerbl M, Steinlechner M, Putz R. Stress distribution in the trochlear notch. A model of bicentric load transmission through joints. J Bone Joint Surg Br 1994;76:647-53.
5. Fick R. Mechanik des gelenkes. In: Handbuch del Anatomie und Mechanik der Gelenke. Jena: Gustav Fischer; 1911.
6. Goel VK, Singh D, Bijlani V. Contact areas in human elbow joints. J Biomech Eng 1982;104:169-75.
7. Goodfellow JW, Bullough PG. The pattern of ageing of the articular cartilage of the elbow joint. J Bone Joint Surg Br 1967; 49:175-81.
8. Ishikawa J, Niebur GL, Uchiyama S, et al. Feasibility of using a magnetic tracking device for measuring carpal kinematics. J Biomech 1997;30:1183-6.
9. Kirstukas SJ, Lewis JL, Erdman AG. 6R instrumented spatial linkages for anatomical joint motion measurement-part 1: design. J Biomech Eng 1992;114:92-100.
10. Kirstukas SJ, Lewis JL, Erdman AG. 6R instrumented spatial linkages for anatomical joint motion measurement-part 2: calibration. J Biomech Eng 1992;114:101-10.
11. Kobayashi M, Berger RA, Nagy L, et al. Normal kinematics of carpal bones: a three dimensional analysis of carpal bone motion relative to the radius. J Biomech 1997;30:787-93.
12. London JT. Kinematics of the elbow. J Bone Joint Surg Am 1981; 63:529-35.
13. Lorensen W, Cline H. Marching cubes: a high resolution 3D surface construction algorithm. Comput Graph 1987;21:163-9.
14. Moritomo H, Viegas SF, Elder KW, et al. Scaphoid nonunions: a 3-dimensional analysis of patterns of deformity. J Hand Surg [Am] 2000;25:520-8.
15. Moritomo H, Viegas SF, Elder K, et al. The scaphotrapeziotrapezoidal joint. Part 2: A kinematic study. J Hand Surg [Am] 2000;25:911-20.
16. Morrey BF, Chao EY. Passive motion of the elbow joint. J Bone Joint Surg Am 1976;58:501-8.
17. Panjabi MM, Krag MH, Goel VK. A technique for measurement and description of three-dimensional six degree-of-freedom mo-

tion of a body joint with an application to the human spine. J Biomech 1981;14:447-60.
18. Patterson RM, Nicodemus CL, Viegas SF, Elder KW, Rosenblatt J. High-speed, three-dimensional kinematic analysis of the normal wrist. J Hand Surg [Am] 1998;23:446-53.
19. Ruby LK, Cooney WP, An KN, Linscheid RL, Chao EY. Relative motion of selected carpal bones: a kinematic analysis of the normal wrist. J Hand Surg [Am] 1988;13:1-10.
20. Savelberg HH, Otten JD, Kooloos JG, Huiskes R, Kauer JM. Carpal bone kinematics and ligament lengthening studied for the full range of joint movement. J Biomech 1993;26:1389-402.
21. Stormont TJ, An KN, Morrey BF, Chao EY. Elbow joint contact study: comparison of techniques. J Biomech 1985;18:329-36.
22. Tanaka S, An KN, Morrey BF. Kinematics and laxity of ulnohumeral joint under valgus-varus stress. J Musculoskeletal Res 1998; 2:45-54.
23. Valero-Cuevas FJ, Small CF. Load dependence in carpal kinematics during wrist flexion in vivo. Clin Biomech 1997;12:154-9.
24. Youm Y, Dryer RF, Thambyrajah K, Flatt AE, Sprague BL. Biomechanical analyses of forearm pronation-supination and elbow flexion-extension. J Biomech 1979;12:245-55.

Patterns of Bone Defect in Scaphoid Nonunion: A 3-Dimensional and Quantitative Analysis

Kunihiro Oka, MD, Tsuyoshi Murase, MD, PhD, Hisao Moritomo, MD, PhD, Akira Goto, MD, Kazuomi Sugamoto, MD, PhD, Hideki Yoshikawa, MD, PhD, ***Osaka, Japan***

Purpose: To clarify patterns and size of bone defect in scaphoid nonunion in order to facilitate accurate correction of scaphoid deformity.

Methods: Three-dimensional computed tomography was used to examine 24 patients with scaphoid nonunion. Configuration and size of bone defect were quantified and computed on the basis of fracture location. Cases were categorized as distal or proximal based on location of the fracture line relative to the dorsal apex of the scaphoid ridge.

Results: Distal scaphoid fractures displayed wedge-shaped bone defects with the base facing volarly. Proximal scaphoid fractures exhibited flat, crescent-shaped defects that presented only around the fracture site. The size of bone defects was significantly greater for distal fractures than for proximal fractures.

Conclusions: Whether the fracture line passes distal or proximal to the dorsal apex of the scaphoid ridge is a crucial factor in the generation of bone defect. A large wedge-shaped bone graft from the volar side is necessary for distal nonunion whereas a small cancellous bone graft from the dorsal side may be preferable for proximal nonunion. (J Hand Surg 2005;30A:359–365. Copyright © 20052005 by the American Society for Surgery of the Hand.)

Key words: Scaphoid nonunion, bone defect, computed tomography.

In scaphoid nonunion restoration of the normal anatomic shape is believed to improve postsurgical function of the wrist joint.[1–7] Correction of scaphoid deformity remains problematic, however, because of the difficulty in detecting accurately the displacement pattern and size of bone defect. Plain radiography does not always provide adequate information about deformity patterns because of the overlapping carpal bones and complicated 3-dimensional (3D) structure of the scaphoid itself. Belsole and Hess[8] quantified angular deformity in fracture fragments from scaphoid waist nonunions. They also calculated the volume of bone defect and estimated the shape by creating 3D computer models. Amount of lost scaphoid bone was 6% to 15% and the shape was a triangular prism. None of these articles, however, reported frac-

From the Department of Orthopaedic Surgery and Department of Medical Robotics and Image Sciences, Osaka University Graduate School of Medicine, Suita, Osaka, Japan.

Received for publication July 15, 2004; accepted in revised form October 7, 2004.

No benefits in any form have been received or will be received from a commercial party related directly or indirectly to the subject of this article.

Reprint requests: Kunihiro Oka, MD, Dept of Orthopaedic Surgery, Osaka University Graduate School of Medicine, 2-2, Yamada-oka, Suita, Osaka 565-0871, Japan.

0363-5023/05/30A02-0019$30.00/0
doi:10.1016/j.jhsa.2004.10.004

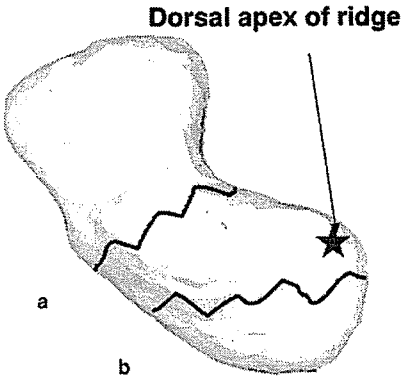

Figure 1. Fracture location of scaphoid nonunion with (A) the distal-type and (B) the proximal-type nonunions. Dorsal view of the right scaphoid.

ture displacement or bone defects on the basis of fracture location.

Nakamura et al[9] categorized deformities of scaphoid nonunion into 2 different types based on direction of the displacement: volar, in which the distal fragment overlaps the proximal fragment volarly; and dorsal, in which the distal fragment overlaps the proximal fragment dorsally. They also reported that the volar type was accompanied frequently by dorsal intercalated segment instability deformity and was often identified when fractures were distal. Conversely the dorsal type was noted frequently when fractures were proximal. Moritomo et al[10] suggested that fracture location volar or dorsal in scaphoid nonunion affects the pattern of deformity. They measured fracture location based on the anatomic landmark of the dorsal apex of the scaphoid ridge, where the dorsal intercarpal ligament and dorsal part of the dorsal scapholunate interosseous ligament attach. Fracture lines were generally distal to the dorsal apex of the scaphoid ridge in the volar type and proximal in the dorsal type (Fig. 1).

The present study aimed to quantify the configuration and size of bone defect based on fracture location to facilitate accurate correction of scaphoid deformity.

Materials and Methods

We studied 24 patients (20 men, 4 women) with established scaphoid nonunion who were seen between 2000 and 2004 at our institution. Mean patient age was 35 years (range, 18–75 years). Mean interval between injury and examination was 83 months (range, 3–480 months). Fourteen patients had sought no treatment for the original fracture and 6 patients had been misdiagnosed with simple sprain; their fractures had not been immobilized. A cast had been used for 3 patients and 1 patient had bone grafting without internal fixation for the fractured scaphoid. The 24 scaphoid nonunions were divided into 2 groups according to the classification of Moritomo et al[10] using 3D modeling. Distal fracture was considered present (n = 20) if the fracture line was distal to the dorsal apex of the scaphoid ridge whereas proximal fracture was considered present (n = 4) if the line was proximal to this landmark (Fig. 1). Mean interval from injury to examination was 88 months (range, 3–480 months) for distal fracture and 59 months (range, 9–93 months) for proximal fracture.

Image Acquisition

Computed tomography (CT) was performed with both wrists fixed using an orthosis in a neutral position with a slice thickness of 0.625 mm (High Speed Advance or LightSpeed Ultra 16, General Electric, Waukesha, WI) and the patient in a prone position with arms elevated over the head. Data were saved in Digital Imaging and Communications in Medicine (DICOM) format, which is used commonly for transferring and storing medical images.

Segmentation and Construction of 3D Surface Bone Model

Segmentation is defined as extracting bone regions and associating each region with individual bones. The anatomic structure or region of interest must be delineated and separated so that it can be viewed individually and 3D bone models can be reconstructed. Regions of individual bones were segmented semiautomatically using software developed in our laboratory (Virtual Place-M, Medical Imaging Laboratory, Tokyo, Japan). We obtained surface models of both distal and proximal segments of the scaphoid by applying 3D surface generation of the bone cortex. Using a graphics workstation we obtained 3D geometry of each bone by connecting different sections. The software generated 3D surface bone models using the marching cubes technique.[11]

Surface-Based Registration

To measure bone defects of the scaphoid we referred to the method of Belsole and Hess[8] to construct the original shape of the fractured scaphoid and the fracture gap by using the opposite scaphoid as a template. Distal and proximal fragment models of scaphoid nonunion were matched to mirror images of the contralateral normal scaphoid model using indepen-

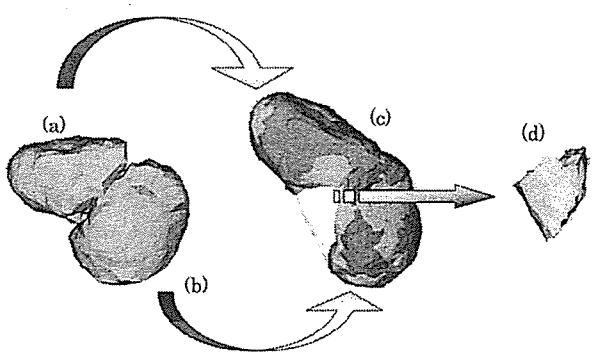

Figure 2. How to calculate bone defect. The distal fragment (a) and the proximal fragment (b) were matched to the mirror image of the contralateral normal scaphoid (c). The bone defect (d) was calculated by subtracting (a) and (b) from (c).

dent implementation of the iterative closest point registration algorithm (Fig. 2).[12] In this method a 3D surface model and set of 3D points are registered by starting from initial transformation parameters and finding finally the optimal parameters while minimizing the sum of the distance from each 3D point to the surface.

Evaluation of Shape and Amount of Bone Defect

The shape of the bone defect was shown by subtracting the reduced nonunion model from the mirror image of the contralateral normal scaphoid using a Boolean operation in commercially available software (Magics RP, Materialise, Leuven, Belgium). The shape of the bone defect was visualized and the amount of bone loss was calculated using the bone defect model. Mean volume of the contralateral normal scaphoid was 2896 mm^3 (range, 2100–4060 mm^3). The ratio of the volume of bone defect to the whole volume of the contralateral scaphoid was calculated.

The shape and volume of the bone defect in each type were compared and the relations of the amount

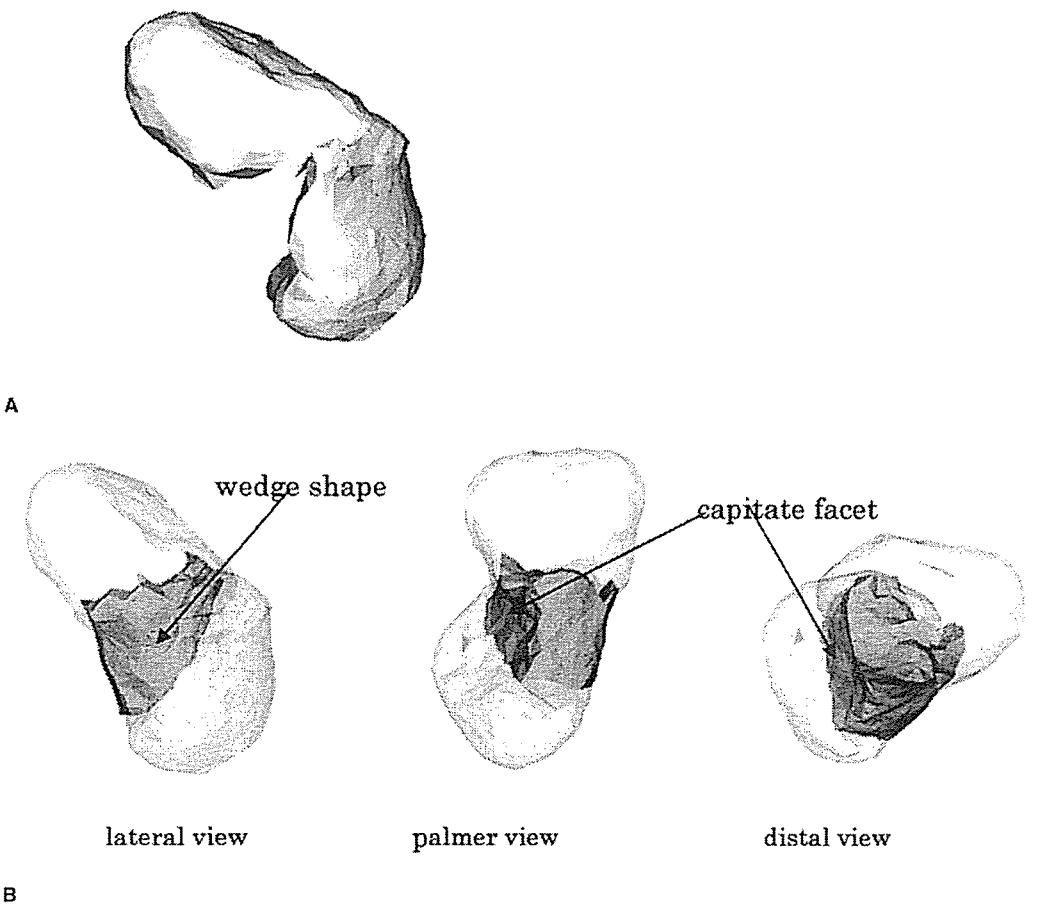

Figure 3. Bone defect in distal-type nonunion. (A) Lateral view of the scaphoid nonunion in the distal type after correction of the deformity. (B) The bone defect in distal type is wedge shaped.

of bone defect to the interval from injury and the occupation were evaluated.

Results

In distal scaphoid fracture all 20 patients displayed the same pattern of bone defect; a wedge shape with the base facing the volar side (Fig. 3). The mean volume of bone defect was 269 mm^3 and the mode was 150 mm^3. The mean ratio of the volume of bone defect to the whole volume of the contralateral normal scaphoid was 9% (range, 3%–19%). In proximal scaphoid fractures all 4 patients had minor bone defects around the fracture site that had a flat, crescent-shaped configuration (Fig. 4). Most proximal fractures showed osteophyte formation on the ridge. The mean volume of bone defect was 26 mm^3 and the mode was 20 mm^3. The mean ratio of the volume of bone defect to the whole volume of the contralateral normal scaphoid was 1% (range, 0.3%–2%). The amount of bone defect was significantly greater in distal fractures than in proximal fractures ($p < .01$). In the proximal fracture bone resorption was not marked even for cases involving long-standing nonunion (Fig. 5). The relations of the amount of bone defect to the interval from injury and occupation are shown in Table 1. We defined intervals from injury origin of less than 12 months as short duration and those of more than 12 months as long duration. Even in patients with distal scaphoid fracture who had short duration the mean amount of bone defect was greater than 100 mm^3 (Fig. 5). The amount of bone defect was not significantly different between the short duration and the long duration injuries. As for the occupation 18 patients worked in nonmanual labor and 6 in manual labor. The amount of bone defect was not significantly different between nonmanual labor and manual labor.

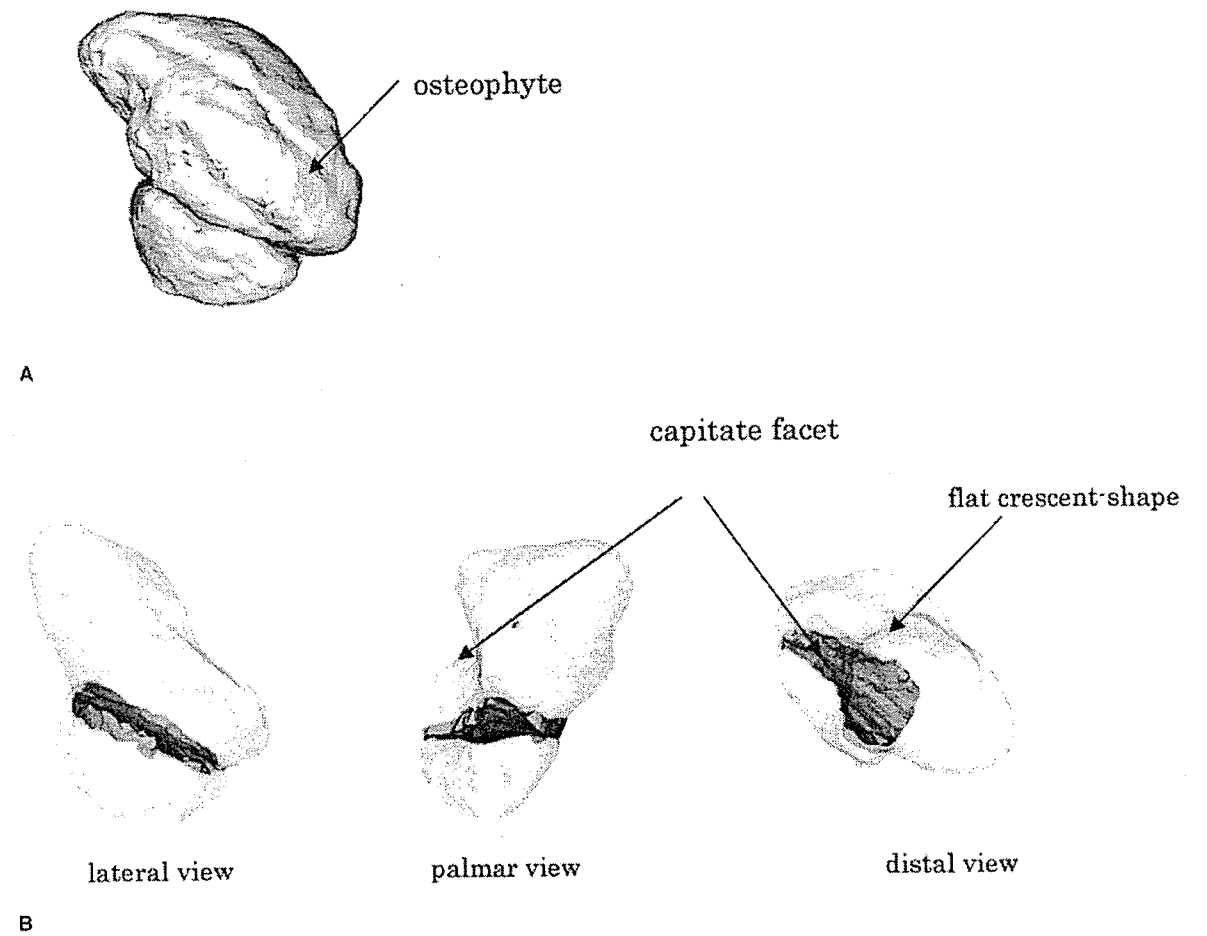

Figure 4. Bone defect in proximal-type nonunion. (A) Lateral view of the scaphoid nonunion in the proximal type. Osteophyte formation is observed on the dorsal ridge. (B) Configuration of the bone defect in the proximal type is a flat crescent shape.

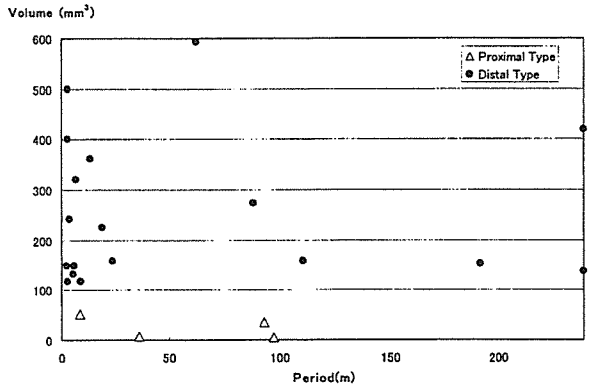

Figure 5. The relationship between the duration of nonunion and the amount of bone defect.

Discussion

Previous studies have emphasized the importance of fracture reduction, rigid fracture internal fixation, and correction of humpback deformity in the treatment of scaphoid nonunion.[13–14] Amadio et al[15] investigated wrist function after scaphoid fracture and concluded that malunited scaphoid fractures with remaining humpback deformity show unsatisfactory clinical results and a predisposition toward degenerative arthritis. In correcting deformities, acquisition of accurate presurgical information regarding the deformity is essential. Fernandez[4] described an anterior wedge-shaped bone defect that was evaluated by comparison with radiographic images of the contralateral normal scaphoid. Cooney et al[3] calculated angulation of the scaphoid using tomography. Sanders[16] estimated humpback deformity using CT along the true longitudinal axis of the scaphoid. They emphasized the importance of restoring anatomic length and configuration of the scaphoid. Belsole et al[8] calculated the angular relationship of the fracture components and the volume of the bone defect by superimposing the computer images of normal and contralateral fractured scaphoids and concluded that the proximal fragment is extended, radially deviated, and supinated in relation to the distal fragment. The amount of scaphoid bone defect varied between 6% and 15% and the configuration of missing bone was a triangular prism with its base facing palmarly. The 3D technique we used is basically the same as that used by Belsole et al. None of these articles, however, reported correlations between deformity and fracture location. Nakamura et al[9] reported that patterns of deformity in scaphoid nonunions could be categorized into 2 types based on 3D CT modeling: (1) fractures in which the distal fragment is displaced dorsally and (2) fractures involving volar displacement. Moritomo et al[10] evaluated these types of displacement in terms of anatomic points. They measured fracture location based on the anatomic landmark of the dorsal apex of the scaphoid ridge.

In this study bone defects in scaphoid nonunion were quantified based on fracture location. The shape and amount of bone defect differ between the 2 fracture types. In distal scaphoid fractures the scaphoid forms a humpback deformity and the bone defects are large and triangular. In proximal fractures the bone defects are much smaller and a flat, crescent-shaped pattern is seen. These results suggest that the location of the fracture line relative to the dorsal apex of the scaphoid ridge represents an important factor in the development of deformity of scaphoid fragments and development of bone defect. The location of the dorsal apex of the scaphoid ridge coincides with the location of the proximal part of the dorsal intercarpal ligament and the dorsal component of the scapholunate interosseous ligament, which are believed to play roles in the dorsal stability of the scaphoid. In proximal fractures ligamentous attachments remain on the distal fragment, possi-

Table 1. The Relations of Period and Occupation to Bone Defect

	Bone Defect (mm³)	Period (mo)
Proximal Fracture		
1	53	9
2*	8	36
3	36	93
4	6	97
Distal fracture		
1	150	3
2	400	3
3*	117	3
4	500	3
5	243	4
6	132	6
7	149	6
8	321	7
9	118	9
10*	362	13
11	225	19
12	159	24
13*	593	62
14	273	88
15*	159	111
16*	153	192
17	420	240
18	138	240
19	483	245
20	286	480

*Manual labor.